

# Simulation Study of Alfvén-Eigenmode-Induced Energetic Ion Transport in LHD<sup>\*)</sup>

Seiya NISHIMURA, Yasushi TODO, Donald A. SPONG<sup>1)</sup>,  
Yasuhiro SUZUKI and Noriyoshi NAKAJIMA

*National Institute for Fusion Science, Toki 509-5292, Japan*

<sup>1)</sup>*Oak Ridge National Laboratory, Oak Ridge, Tennessee 37831, USA*

(Received 22 November 2012 / Accepted 22 April 2013)

The interaction between toroidal Alfvén eigenmode (TAE) and energetic ions in the Large Helical Device (LHD) is investigated using a reduced version of the MEGA code that implements a realistic equilibrium magnetic field with the HINT code and corresponding TAE profile with the AE3D code. In simulations, the linear growth rate of TAE amplitude is proportional to energetic ion density; consequently, the nonlinear saturation level of the TAE amplitude is enhanced by the increase in the energetic ion density. Energy transfer analysis is performed to clarify destabilization and saturation mechanisms of the TAE and to identify resonant energetic ions. An analysis of test particles in the electromagnetic field perturbed by the TAE shows that the magnitude of fluctuations in the energetic ion orbits is proportional to the square root of the TAE amplitude. Our results qualitatively reproduce the radial transport of energetic ions by the TAE in the LHD.

© 2013 The Japan Society of Plasma Science and Nuclear Fusion Research

Keywords: Alfvén eigenmode, energetic ion, three-dimensional equilibrium, hybrid simulation, particle-in-cell method

DOI: 10.1585/pfr.8.2403090

## 1. Introduction

To achieve magnetic confinement fusion, the interaction between Alfvén eigenmodes and energetic ions is an important issue to be resolved [1]. In the Large Helical Device (LHD), which is a stellarator, bursts of toroidal Alfvén eigenmode (TAE) and associated energetic ion transport and losses have been observed during neutral beam injection [2]. TAE-induced energetic ion transport has been investigated in axisymmetric systems such as tokamaks [3], but that in stellarators relies on an analogy with tokamaks and is not yet fully described. In this paper, we approach this problem using a *reduced* version of the MEGA code [4–6]. In this code, data from the HINT code [7, 8], which solves the resistive magnetohydrodynamic (MHD) equations, is used to obtain the realistic equilibrium magnetic field in the LHD. The TAE spatial profile in the equilibrium field is given by the AE3D code [9], which solves the reduced MHD equations for stellarators [9–11]. The energetic ion orbits in the superposition of the equilibrium and perturbed fields are calculated by the particle-in-cell method with the so-called  $\delta f$  method [12]. Using the code, the time evolution of the TAE amplitude and the consequent energetic ion transport in the LHD are simulated.

This paper is organized as follows. In §2 and §3, we briefly introduce the simulation model. In §4, the linear growth rate of the TAE and the nonlinear saturation level

of the TAE amplitude are surveyed. In §5, the magnitude of the fluctuation in energetic ion orbits due to the TAE is investigated by test particle analysis. Finally, a summary is presented in §6.

## 2. Data from HINT and AE3D Codes

The HINT code and AE3D code employ the Boozer coordinates  $(\rho_\psi, \vartheta, \zeta)$  are employed, where  $\rho_\psi \propto \sqrt{\psi_1}$  is the normalized minor radial position,  $\psi_1$  is the toroidal magnetic flux,  $\vartheta$  is the effective poloidal angle, and  $\zeta$  is the effective toroidal angle. In the MEGA code, data described by the Boozer coordinates are converted to the cylindrical coordinates  $(R, \phi, Z)$ , where  $R$  is the major radial position,  $\phi$  is the toroidal angle, and  $Z$  is the vertical position.

Figure 1 shows (a) the poloidal cross section of the equilibrium magnetic field in the LHD at different toroidal angles,  $\phi = 0$  [rad] and  $\phi = \pi/10$  [rad], and (b) the radial profile of the rotational transform. In the LHD, helically wound coils have a pole number (symmetry number in the poloidal direction) of  $l = 2$  and a pitch number (symmetry number in the toroidal direction) of  $M = 10$ . The average minor radius is approximately  $a = 60$  [cm]. Because the AE3D code requires a nested magnetic surface, the VMEC code [13] is also used to construct the nested equilibrium magnetic field which is comparable to that in Fig. 1.

Figure 2 shows the Alfvén continua of the  $n = 1$  mode family calculated by AE3D. Many eigenmodes are observed in Fig. 2, but we focus on the TAE with  $n = 1$  and  $m = 0, 1, 2$ , and 3 for the reduced simulation, which

author's e-mail: nishimura.seiya@lhd.nifs.ac.jp

<sup>\*)</sup> This article is based on the presentation at the 22nd International Toki Conference (ITC22).

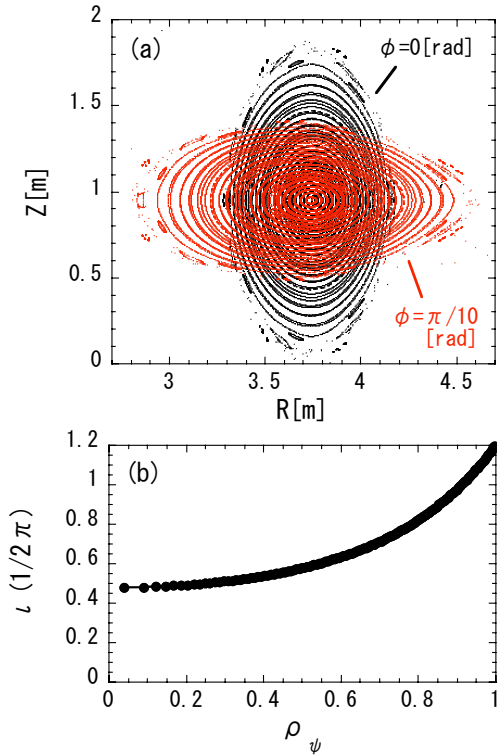


Fig. 1 Equilibrium magnetic field in LHD calculated by the HINT code: (a) Poincaré plots of equilibrium magnetic field at toroidal angles  $\phi = 0$  [rad] and  $\phi = \pi/10$  [rad] and (b) radial profile of rotational transform in the Boozer coordinates.

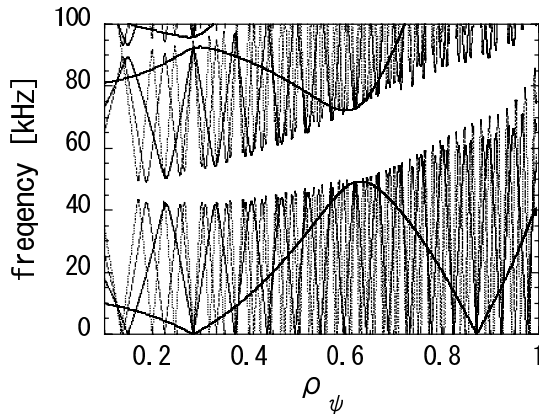


Fig. 2 Alfvén continua of  $n = 1$  mode family calculated by AE3D.

corresponds to the slowly changing bold curves, where  $n$  is the toroidal mode number and  $m$  is the poloidal mode number.

Figure 3 shows the radial profile of the electrostatic potential of the TAE for modes with frequencies of (a) 51.3 [kHz] and (b) 71.5 [kHz]. In both modes,  $(m, n) = (1, 1)$  and  $(m, n) = (2, 1)$  are dominant. Those modes are located inside the continuum gap owing to the toroidal coupling of the  $(1, 1)$  and  $(2, 1)$  modes. In AE3D, the boundary condition with the perfect conductor is used [9]; that is, the

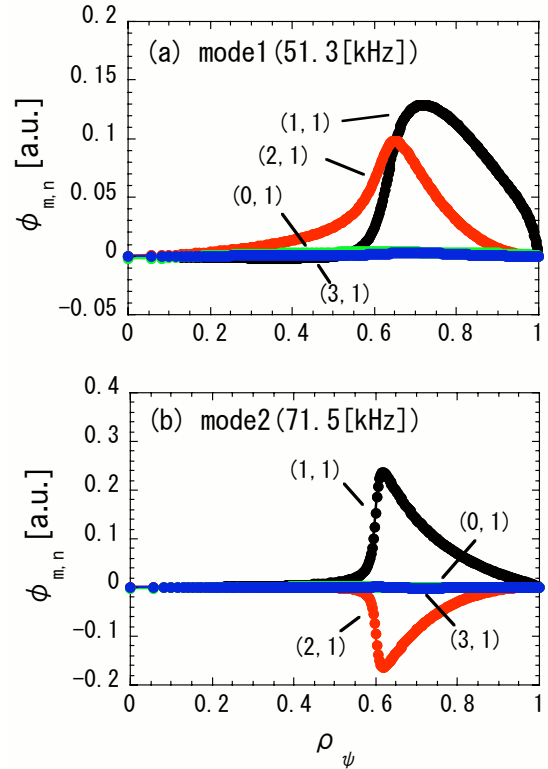


Fig. 3 Radial profile of the electrostatic potential of TAE calculated by AE3D for modes with frequencies of (a) 51.3 [kHz] and (b) 71.5 [kHz].

electrostatic potential perturbation is zero at  $\rho_\psi = 1$ , which might give rise to rapid radial decay of 51.3 [kHz]  $(1, 1)$  mode at the edge boundary.

The rotation frequency of the shear Alfvén wave is given by  $\omega_{m,n} = \pm k_{\parallel m,n} v_A$ , where  $k_{\parallel m,n} = (1/R_0)(m - n)$  is the parallel wave number,  $R_0$  is the major radial position of the magnetic axis,  $v_A$  is the Alfvén velocity, and the sign indicates the direction of propagation. The resonance condition,  $\omega_{1,1} = -\omega_{2,1}$  determines the center of the gap as  $\iota = 2/3$  at the radial position of  $\rho_\psi = 0.65$  [see Fig. 1 (b)], which is close to the peaks of the eigenfunctions in Fig. 3. Around  $\rho_\psi = 0.65$ , a gap in the eigenfrequency forms, where the frequencies at the lower and upper accumulation points are 49.5 [kHz] and 72.0 [kHz], respectively.

### 3. Simulation Model

The nonlinear energetic ion dynamics are determined by the electromagnetic field, which is the sum of the equilibrium field and TAE perturbation. The energetic ions are represented by marker particles, and the electromagnetic field at the particle position is given by the particle-in-cell method with linear interpolation.

The time evolution of the guiding center velocity of energetic ions,  $v_{gc}$ , is determined by the drift-kinetic velocity model in Ref. [14], which is the summation of the modified parallel velocity (partially including the curvature

drift velocity),  $E \times B$  drift velocity, curvature drift velocity, and  $\nabla B$  drift velocity:

$$\begin{aligned} \mathbf{v}_{gc} &= \mathbf{v}_{\parallel}^* + \mathbf{v}_E^* + \mathbf{v}_c^* + \mathbf{v}_B^* \\ &= \frac{v_{\parallel} B}{B_{\parallel}^*} \mathbf{b} + \frac{1}{B_{\parallel}^*} \mathbf{E} \times \mathbf{b} + \frac{\rho_{\parallel} v_{\parallel} B}{B_{\parallel}^*} \nabla \times \mathbf{b} \\ &\quad - \frac{\mu}{q_{ep} B_{\parallel}^*} \nabla B \times \mathbf{b}. \end{aligned} \quad (1)$$

The original velocity parallel to the magnetic field line,  $v_{\parallel}$ , obeys the evolution equation:

$$m_{ep} \frac{dv_{\parallel}}{dt} = \frac{B^*}{B_{\parallel}^*} \cdot (q_{ep} \mathbf{E} - \mu \nabla B), \quad (2)$$

where  $\mathbf{E}$  is the electric field,  $\mathbf{b}$  is the unit vector of the magnetic field,  $B$  is the magnitude of the magnetic field,  $B_{\parallel}^* = B(1 + \rho_{\parallel} \mathbf{b} \cdot \nabla \times \mathbf{b})$  is the magnitude of the effective parallel magnetic field,  $\rho_{\parallel} = m_{ep} v_{\parallel} / q_{ep} B$  is the parallel Larmor radius,  $\mu = m_{ep} v_{\perp}^2 / 2B^2$  is the magnetic moment,  $m_{ep}$  is the energetic ion mass,  $q_{ep}$  is the charge, and  $v_{\perp}$  is the perpendicular velocity. The equilibrium energetic ion distribution function  $f_0$  is modeled by coupling the Gaussian, and slowing-down distributions [15] such that  $f_0 \propto \exp(-\rho_{\psi}^2 / \delta \rho_{\psi}^2) / (v^3 + v_c^3) \text{erfc}((v - v_0) / \delta v)$ , where  $v$  is the absolute value of the energetic ion velocity and the complementary error function is defined as  $\text{erfc}(s) = (1 / \sqrt{\pi}) \int_s^{\infty} \exp(-t^2) dt$ , where  $s$  is arbitrary. In the simulations, we choose  $\delta \rho_{\psi} = 0.4$ ,  $v_c / v_A = 0.5$ ,  $v_0 / v_A = 1.18$ , and  $\delta v / v_A = 0.1$ . The numerical factor of  $f_0$  is specified when we choose the energetic ion density at the plasma center. The initial distribution of the pitch angle parameter  $\lambda = v_{\parallel} / v$  is assumed to be isotropic in  $v_{\parallel} - v_{\perp}$  space, where  $v = \sqrt{v_{\parallel}^2 + v_{\perp}^2}$ .

The electric field and the magnetic field perturbed by the TAE are given by  $\mathbf{E} = \mathbf{E}_c + \mathbf{E}_s = -\nabla_{\perp} (\Phi_s + \Phi_c)$  and  $\mathbf{B} = \mathbf{B}_0 + \nabla \times [(A_{\parallel s} + A_{\parallel c}) \mathbf{b}]$ , respectively, where  $\mathbf{B}_0$  is the equilibrium magnetic field given by the HINT code. The sine and cosine components of the electrostatic potential perturbation and the parallel vector potential perturbation are modeled by  $\Phi_s = X \sum_{m,n} \phi_{m,n} \sin \Theta$ ,  $\Phi_c = Y \sum_{m,n} \phi_{m,n} \cos \Theta$ ,  $A_{\parallel s} = X \sum_{m,n} a_{\parallel m,n} \sin \Theta$ , and  $A_{\parallel c} = Y \sum_{m,n} a_{\parallel m,n} \cos \Theta$ , respectively, where  $\Theta = m\vartheta - n\zeta - \omega t$ ,  $\omega$  is the eigenfrequency given by AE3D,  $\{\phi_{m,n}, a_{\parallel m,n}\}$  are the eigenfunctions given by AE3D, and  $\{X, Y\}$  are the time-dependent amplitudes. The rate of increase in the energetic ion energy is given by  $\langle \mathbf{j}_{ep} \cdot \mathbf{E} \rangle$ , where  $\mathbf{j}_{ep}$  is the energetic ion current due to the curvature drift and  $\nabla B$  drift, and the bracket indicates the volume integral. In the  $\delta f$  method, the volume integral  $\langle \mathbf{j}_{ep} \cdot \mathbf{E} \rangle$  is calculated by summing each particle's contribution multiplied by a weight function [4, 12]. The weight function is defined as the product of the distribution function perturbation and the phase-space volume filled by each particle, and the evolution equation of the weight function is based on the perturbed Vlasov equation. The stored energies of the sine

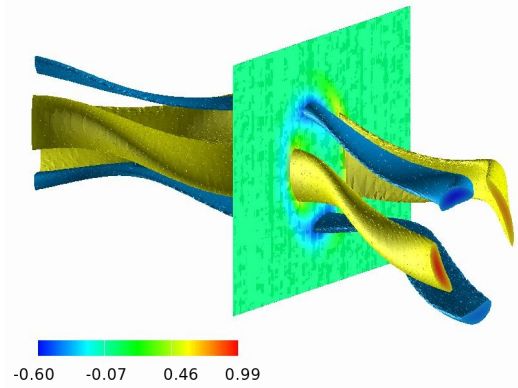


Fig. 4 Contour and isosurface plots of the electrostatic potential of the TAE by the AE3D code implemented in the MEGA code (arbitrary units).

and cosine components of the TAE,  $W_s$  and  $W_c$ , are proportional to  $X^2$  and  $Y^2$ , respectively. Then, the energy conservation law yields the following relations

$$\frac{1}{X} \frac{dX}{dt} = -\frac{1}{W_s} \langle \mathbf{j}_{ep} \cdot \mathbf{E}_s \rangle, \quad (3)$$

$$\frac{1}{Y} \frac{dY}{dt} = -\frac{1}{W_c} \langle \mathbf{j}_{ep} \cdot \mathbf{E}_c \rangle. \quad (4)$$

Figure 4 shows the implementation of the TAE data by the AE3D code in the MEGA code. An example of a contour plot of the electrostatic potential of the TAE in the poloidal plane and isosurface plots are shown. Note that the rippled structure in Fig. 4 is due to the helically wound equilibrium magnetic field.

In the following simulations, the number of marker particles is  $6.6 \times 10^5$ , and the pitch angle parameter  $\lambda$  of each marker particle in the initial distribution is determined by a pseudo random number generator.

## 4. Simulation Results

The plasma parameters for the following simulations are  $B_{eq} = 0.5$  [T] and  $n_{eq} = 8.9 \times 10^{18}$  [m<sup>-3</sup>], where  $B_{eq}$  is the maximum toroidal magnetic field and  $n_{eq}$  is the maximum plasma density.

Figure 5 shows the energetic ion density dependence of the linear growth rate of the TAE for the two modes in Fig. 3. The linear growth rate is clearly proportional to the energetic ion density. Earlier analytical work showed that the linear growth rate of the TAE in stellarators is proportional to the  $\beta$  value of energetic ions [17]. In particular, the linear dependence of the linear growth rate on the energetic ion density shown in Eq. (40) in Ref. [17] is consistent with our simulation results. However, the dependence on the temperature is not easily checked because the leading order of the energetic ion distribution function is nonMaxwellian. Alternatively, it is confirmed that the linear growth rate is a monotonically increasing function of the maximum velocity close to the value of  $v_0$  and is not

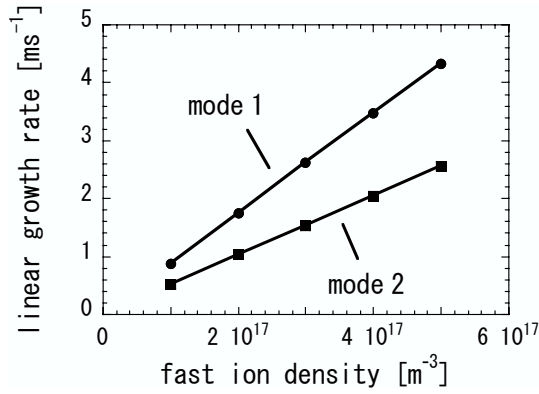


Fig. 5 Dependence of the linear growth rate of the TAE on the energetic ion density at the plasma center.

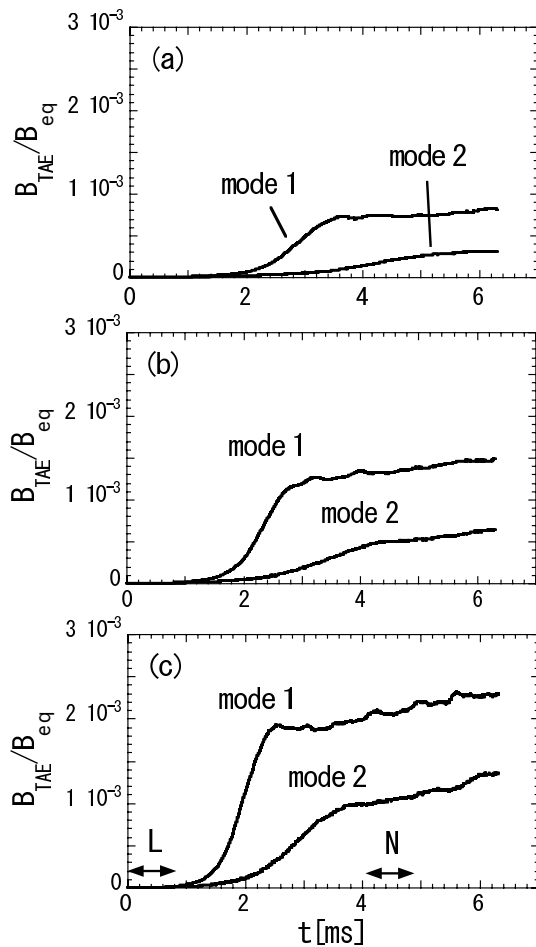


Fig. 6 Time evolution of TAE amplitude with different values of the energetic ion density at the plasma center: (a)  $3 \times 10^{17} \text{ m}^{-3}$ , (b)  $4 \times 10^{17} \text{ m}^{-3}$ , and (c)  $5 \times 10^{17} \text{ m}^{-3}$ .

sensitive to the values of  $v_c$  and  $\delta v$ .

Figure 6 shows the time evolution of the TAE amplitude, where the maximum amplitude of the magnetic field due to the TAE perturbation is represented by  $B_{\text{TAE}}$ . In the early phase, exponential growth of the mode amplitude is observed. The TAE growth enters the nonlinear phase

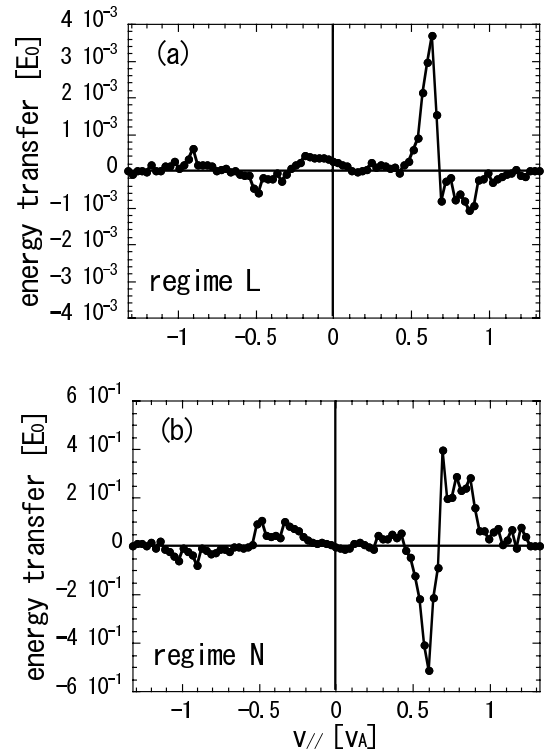


Fig. 7 Parallel energetic ion velocity spectrum of energy transfer from energetic ions to the low frequency TAE (mode1) in the (a) linearly growing regime and (b) nonlinearly growing regime, corresponding to Fig. 6(c), where  $E_0 = 85.1 \text{ [J]}$  is a normalization parameter.

when the mode amplitude becomes sufficiently large. The saturation amplitude increases monotonically with the energetic ion density. The oscillatory behavior of the mode amplitude in the saturation phase is due to particle trapping by the TAE, which interrupts the energy exchange among particles and waves, giving rise to the saturation of the mode growth [16]. In fact, the oscillation of the mode amplitude in the saturation phase in Fig. 6 has a time scale on the order of 1 [ms], which is of the same order as the linear growth rate of the TAE. After the first nonlinear saturation, the mode growth gradually continues. It is also confirmed that the TAE frequency does not vary by more than the linear growth rate of the TAE, which is consistent with the constraints imposed by the constant mode structure and equilibrium. In other words, the mode growth rate is much smaller than the mode frequency; thus, the feedback to the mode frequency is negligible.

To identify resonant energetic ions, which drive the linear and nonlinear growth of the TAE, we analyze the energy transfer process. Considering Eqs. (3) and (4), the energy transfer from energetic ions to the TAE is given by  $-\int dt \langle \mathbf{j}_{ep} \cdot (\mathbf{E}_s + \mathbf{E}_c) \rangle$ .

Figure 7 shows the parallel energetic ion velocity spectrum of energy transfer to the low-frequency TAE (mode1), where regimes L and N correspond to those in Fig. 6(c). In the linear (L) regime, energetic ions with a

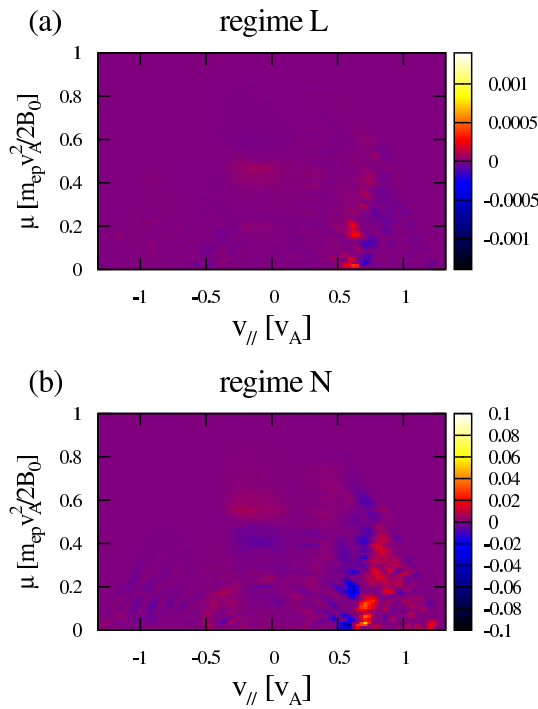


Fig. 8 Parallel energetic ion velocity and magnetic moment spectrum of energy transfer from energetic ions to the low-frequency TAE (mode 1) in the (a) linear growth regime and (b) nonlinear growth regime, corresponding to Fig. 6(c), where the energy is normalized by  $E_0 = 85.1$  [J].

parallel velocity close to  $v_{||} = 0.6 [v_A]$  drive the linear growth of the TAE. In the nonlinear (N) regime, the energy transfer around  $v_{||} = 0.6 [v_A]$  tends to be cancelled out, which might be due to particle trapping caused by the TAE-induced electric field. However, energetic ions with a parallel velocity close to  $v_{||} = 0.3 [v_A]$  and  $0.8 [v_A]$  newly drive the nonlinear growth of the TAE.

Figure 8 shows the parallel energetic ion velocity and magnetic moment spectrum of energy transfer to the low-frequency TAE in regimes L and N. Figures 8(a) and (b) correspond to Figs. 7(a) and (b), respectively. Figure 8 indicates that the resonance parallel velocity depends on the magnetic moment.

Figures 7 and 8 clarify that the gradual growth of the TAE in the nonlinear regime is caused by the shift in the energy source. The trapping of resonant energetic ions with the resonant parallel velocity,  $v_{||}^{res}$ , implies that the TAE-induced field is strong enough to deform the orbits of energetic ions with parallel velocities close to  $v_{||}^{res}$ . Then, the modification of the energetic ion orbit enables the TAE to access a new energy source and triggers nonlinear instability. However, the mechanism of the access to the new energy source is not yet fully understood in detail, although it might be investigated elsewhere. If the inherent damping of the TAE modes is included in Eqs. (3) and (4), it will dominate the weak nonlinear instability observed in our simulation.

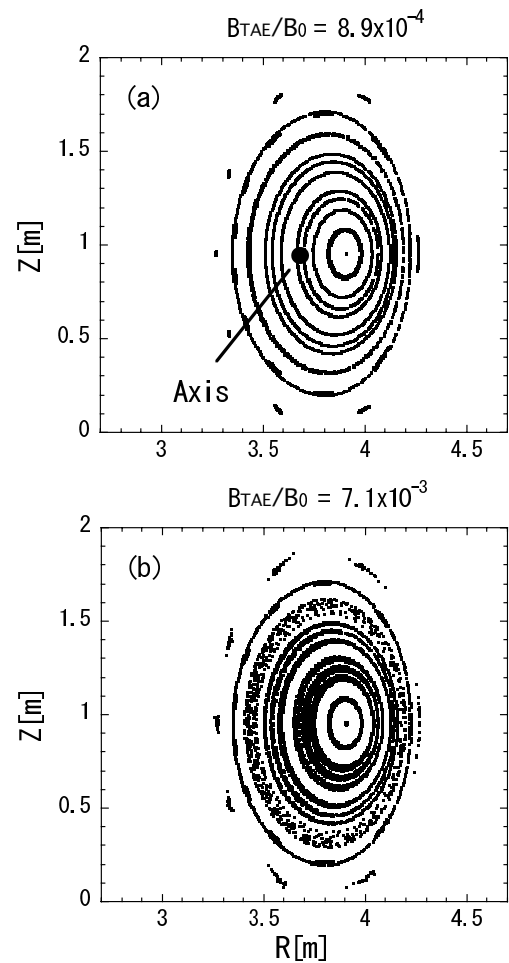


Fig. 9 Poincaré plot of test particles in vertically elongated poloidal planes for (a)  $B_{TAE}/B_{eq} = 8.9 \times 10^{-4}$  and (b)  $B_{TAE}/B_{eq} = 7.1 \times 10^{-3}$ .

## 5. Test Particle Analysis

In the following, we perform the test particle analysis to clarify the energetic ion orbit. The simulation conditions are as follows: the number of test particle is  $10^2$ , and the initial particle velocity is  $v_{||} = v_0 = 1.18v_A$  and  $v_{\perp} = 0$ ; only the low-frequency mode (mode 1) is considered, and the amplitude of the TAE is fixed but the TAE is oscillated with the linear rotation frequency.

Figures 9 and 10 show Poincaré plots of the test particles in the vertically elongated plane ( $\phi = k\pi/5$  [rad]  $k = 0, 1, 2, \dots, 9$ ) and the horizontally elongated poloidal plane ( $\phi = \pi/10 + k\pi/5$  [rad]  $k = 0, 1, 2, \dots, 9$ ), respectively for different values of the TAE amplitude. The axis of the equilibrium magnetic field is shown in Figs. 9(a) and 10(a). In comparison with Fig. 1(a), it is observed that the orbit strongly deviates from the magnetic surface owing to the curvature drift. Note that the  $\nabla B$  drift is absent because only test particles with  $v_{\perp} = 0$  are used, and the condition  $\mu = 0$  holds in the simulation.

Figure 11 shows the maximum orbit width in both horizontally elongated and vertically elongated planes. The

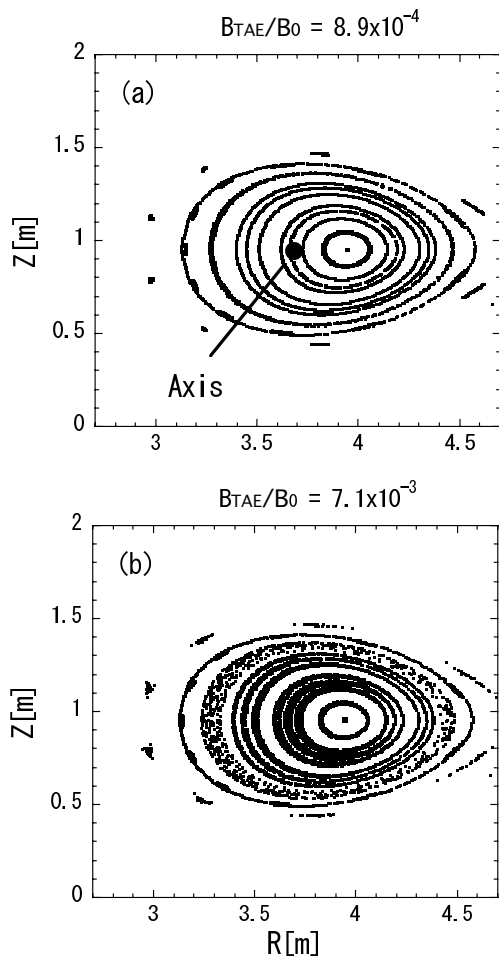


Fig. 10 Poincaré plot of test particles in horizontally elongated poloidal planes for (a)  $B_{\text{TAE}}/B_{\text{eq}} = 8.9 \times 10^{-4}$  and (b)  $B_{\text{TAE}}/B_{\text{eq}} = 7.1 \times 10^{-3}$ .

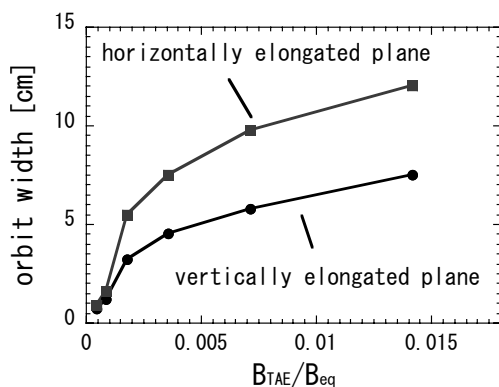


Fig. 11 TAE amplitude dependence of the maximum orbit width of test particles in the horizontally elongated and the vertically elongated planes.

maximum orbit width is measured on the interior equatorial plane. The orbit width in the horizontally elongated plane is approximately 1.6 times of that in the vertically elongated plane. This factor roughly agrees with the aspect ratio of the semi-major axis to the semi-minor axis in

the poloidal cross section,  $\sim 1.8$ , which indicates that the change in the orbit width is due to the toroidal dependence of the magnetic surface shape.

For our simulation condition, we conclude that the orbit width is approximately 10% of the average minor radius when the TAE amplitude  $B_{\text{TAE}}/B_{\text{eq}}$  is in the range between  $10^{-3}$  and  $10^{-2}$ , which is consistent with the results in Ref. [5], using an axisymmetric equilibrium magnetic field comparable to that of the LHD. In LHD experiments, the radial transport of energetic ions sometimes reaches 10% of the average minor radius [2]. A comparison with experimental data is necessary to check the validity of our results; this is left as a future work.

## 6. Summary

In this study, the interaction between the TAE and energetic ions in a realistic equilibrium magnetic field in the LHD was investigated. In the linear growth phase of the TAE, the linear growth rate is proportional to the energetic ion density. In the nonlinear simulations, the saturation level of the TAE amplitude increased with the energetic ion density. Energy transfer analysis identified the resonant energetic ions, which drive the linear instability, first saturation, and nonlinear instability of the TAE. A test particle analysis showed that the magnitude of the fluctuation of energetic ion orbits is proportional to the square root of the TAE amplitude. Simulations of more realistic situations with neutral beam injection and the finite plasma pressure effect are left as future works.

## Acknowledgements

Numerical computations were performed at the Helios at the IFERC-CSC and the Plasma Simulator at the National Institute for Fusion Science. This work was partially supported by a Grant-in-Aid for JSPS Fellows (23-5218).

- [1] W.W. Heidbrink, *Phys. Plasmas* **15**, 055501 (2008).
- [2] M. Osakabe *et al.*, *Nucl Fusion* **51**, 083030 (2011).
- [3] W.W. Heidbrink and G.J. Sadler, *Nucl. Fusion* **34**, 535 (1994).
- [4] Y. Todo *et al.*, *Phys. Plasmas* **10**, 2888 (2003).
- [5] Y. Todo *et al.*, *Plasma Fusion Res.* **3**, S1074 (2008).
- [6] Y. Todo *et al.*, *Fusion Sci. Technol.* **58**, 277 (2010).
- [7] K. Harafuji *et al.*, *J. Comput. Phys.* **81**, 169 (1989).
- [8] Y. Suzuki *et al.*, *Nucl. Fusion* **46**, L19 (2006).
- [9] D.A. Spong *et al.*, *Phys. Plasmas* **17**, 022106 (2010).
- [10] S.E. Kruger *et al.*, *Phys. Plasmas* **5**, 4169 (1998).
- [11] O.P. Fesenyuk *et al.*, *Phys. Plasmas* **9**, 1589 (2002).
- [12] A.Y. Aydemir, *Phys. Plasmas* **1**, 822 (1994).
- [13] S.P. Hirshman and J.C. Whitson, *Phys. Fluids* **26**, 3553 (1983).
- [14] R.G. Littlejohn, *J. Plasma Phys.* **29**, 111 (1983).
- [15] J.G. Cordey and M.J. Houghton, *Nucl. Fusion* **13**, 215 (1973).
- [16] H.L. Berk, B.N. Breizman and M. Pekker, *Phys. Rev. Lett.* **76**, 1256 (1996).
- [17] Ya.I. Kolesnichenko *et al.*, *Phys. Plasmas* **9**, 517 (2002).